PNIPAM-Based Copolymer Microgels as Nanoreactors for the In Situ Synthesis of Gold Nanoparticles

Marius Otten, Diana Hildebrandt, Saskia Mölders, Marco Hildebrandt, Andrij Pich, Matthias Karg

Macromolecular Chemistry and Physics

Macromolecular Chemistry and Physics
www.mcp-journal.de

RESEARCH ARTICLE OPEN ACCESS

PNIPAM-Based Copolymer Microgels as Nanoreactors for the In Situ Synthesis of Gold Nanoparticles

Marius Otten[1] | Diana Hildebrandt[1] | Saskia Mölders[1] | Marco Hildebrandt[1] | Andrij Pich[2,3] | Matthias Karg[1,4]

[1]Institut Für Physikalische Chemie I: Kolloide und Nanooptik, Heinrich-Heine-Universität Düsseldorf, Düsseldorf, Germany | [2]DWI-Leibnitz-Institute For Interactive Materials e.V., Aachen, Germany | [3]Functional and Interactive Polymers, Institute For Technical and Macromolecular Chemistry, RWTH Aachen University, Aachen, Germany | [4]Institut Für Chemie, Physikalische Chemie funktionaler Polymere, Martin-Luther-Universität Halle-Wittenberg, Halle, Germany

Correspondence: Matthias Karg (matthias.karg@chemie.uni-halle.de)

Received: 11 July 2025 | **Revised:** 3 September 2025 | **Accepted:** 8 September 2025

Funding: The authors acknowledge the DFG and the State of NRW for funding the cryo-TEM (INST 208/749-1 FUGG). The authors also would like to thank Déborah Feller (HHU Düsseldorf) for assistance with the surfactant-supported overgrowth protocol. This work benefited from the use of the SasView application, originally developed under NSF award DMR-0520547. SasView contains code developed with funding from the European Union's Horizon 2020 research and innovation programme under the SINE2020 project, grant agreement No 654000.

Keywords: gold nanoparticles | in situ nanoparticle synthesis | nanoreactors | PNIPAM copolymer microgels | thermoresponsive polymers

ABSTRACT

The combination of microgels and inorganic nanoparticles leads to hybrid systems with unique properties that are interesting for catalysis, optics, and biomedicine. A common strategy to incorporate nanoparticles into microgels is through encapsulation via seeded precipitation polymerization, leading to structurally well-defined core-shell microgels. An alternative and highly promising approach is the in situ nanoparticle formation within microgels. While this often leads to a random distribution of many nanoparticles per microgel, a challenge lies in the design of microgels that provide spatial control over nanoparticle formation to enable the formation of single nanoparticles in the central region of the microgels. In this study, we systemically investigate poly-*N*-isopropylacrylamide-based copolymer microgels as versatile nanoreactors for the in situ synthesis of gold nanoparticles. By incorporating the comonomers acetoacetoxyethyl methacrylate (AAEM) and acrylic acid (AAc), we shine light on the role of different functionalities for the in situ reduction and microgel colloidal stability. Importantly, depending on microgel composition and gold ion concentration, it is possible to synthesize single, monodisperse nanoparticles within each microgel. Additionally, we demonstrate that the formed nanoparticles can be overgrown through an easy one-step protocol. Our new hybrid copolymer microgels are colloidally stable and show pronounced deswelling/swelling behavior in response to temperature.

1 | Introduction

Microgels are colloid-like objects with sizes in the colloidal regime and an internal gel-like structure composed of chemically and/or physically crosslinked polymer chains [1]. These soft, deformable objects can react to external stimuli like changes in pH, temperature or ionic strength, which enable the microgels to either swell or de-swell in the surrounding solvent, resulting in a change of their size [2–4]. These characteristics make them attractive systems for different applications like the usage as a carrier for (bio)molecules in medical applications [5–7], responsive coatings [8, 9] as well as smart membranes [10, 11]. The combination of microgels and nanoparticles (NPs) for example, made from gold, silver or silicon dioxide, yields hybrid microgels that can serve as new multifunctional building blocks for photonic and plasmonic applications [12–16]. Due to the internal

gel-like structure and large solvent contents, small molecules can diffuse through the polymeric network, which is the basis for in situ overgrowth of metal cores in core-shell (CS) microgels and the use of hybrid microgels in catalysis [12, 13, 17–25].

Besides microgels homogenously or partially loaded with multiple NPs [26, 27] and microgels that are loaded with NPs in their outer periphery [28–31], especially CS microgels with single NP cores attracted significant interest in sensing [32–34], photonics [35, 36], and catalysis [37, 38]. In contrast to microgels that contain multiple NPs, CS microgels allow for the preparation of 2- and 3D superstructures with single NPs at each lattice point [39–41]. For example, due to pronounced adsorption of microgels to different interfaces, including air/water interfaces, CS microgels with plasmonic cores can be used for the preparation of non-close packed 2D periodic lattices with tailored plasmonic properties [12, 13, 42, 43]. Such structurally well-defined lattices can support plasmonic surface lattice resonances—resonances that are characterized by significantly sharper linewidth compared to the localized surface plasmon resonance (LSPR) of individual NPs or random assemblies of plasmonic NPs [44–46]. Furthermore, the deformability of the soft microgel shells allows for altering the lattice constant in such periodic assemblies by altering the packing fraction, that is, the available area per CS microgel [44, 45, 47]. For the study of the phase behavior of microgels in 3D assemblies, NP cores can provide strong scattering contrast, for example in small-angle X-ray scattering (SAXS), that allows for i) the determination of the number concentration via the forward scattering of the high contrast cores [48], and ii) the separation of form and structure factor that is needed, for example, for the assignment of crystal structures in crystalline assemblies [49, 50]. Such studies rely on monodisperse and well-defined CS microgel building blocks with single NP cores.

The common approach for the preparation of such CS microgels with inorganic NP cores is seeded precipitation polymerization. Here, NP cores are typically surface functionalized and then added to the reaction mixture containing monomers and chemical cross-linkers prior to the polymerization. Upon initiation of the polymerization, growing oligomers will precipitate onto the NP surface, leading to the encapsulation [51]. This approach has been used to encapsulate, for example, silica [49, 52–54] and gold NPs (AuNPs) [17, 36, 51, 55]. The ratio between NPs and monomers in the reaction mixture can be used to tailor the shell-to-core size ratio [54, 56].

Thies et al. presented an interesting alternative for the preparation of CS hybrid microgels through the in situ synthesis of AuNPs within copolymer microgels serving as nanoreactors [57]. The copolymer microgels were prepared from *N*-vinylcaprolactam (VCL) as the main monomer and acrylic acid (AAc) and acetoacetoxy ethyl methacrylate (AAEM) as functional comonomers. The AAEM moieties were found crucial for the localization of the AuNPs in the center of the microgels and the formation of single NPs per microgel. The β-diketone groups of the AAEM are known for their capability of complexing metal ions [58, 59], thus leading to a local concentration of gold ions in the AAEM-rich regions of the microgels prior to the following reduction. The authors have also shown that the plasmonic properties of the obtained CS microgels can be enhanced by the sequential overgrowth of the cores within the microgels.

In this study, we aim to transfer the approach of Thies et al. [57] to PNIPAM-based microgels in order to obtain CS microgels with pronounced temperature-dependent swelling/deswelling behavior in aqueous dispersion. We do this by first evaluating the role of different functional monomers for the colloidal stability of the microgels and for the successful in situ formation of AuNPs. The obtained copolymer microgels were studied by transmission electron microscopy (TEM), temperature-dependent dynamic light scattering (DLS) as well as electrophoretic light scattering measurements. We identified microgel compositions and reaction conditions that yield CS microgels with single AuNP cores that were introduced by in situ reduction using the microgels as nanoreactors. These hybrid microgels are colloidally stable over a broad range of temperature and, at the same time, show the typical volume phase transition (VPT) behavior characteristic to PNIPAM-based microgels. Furthermore, our results reveal a pronounced dependence on the microgel-to-gold ion ratio in the in situ reduction, which directly influences the size and number of formed AuNPs. We show that the formed AuNPs are well-embedded into the microgels. Using growth protocols for the post-modification, the plasmonic properties of our new hybrid microgels can be enhanced through the sequential overgrowth of the AuNP cores. The resulting changes were followed by UV–vis absorbance spectroscopy and SAXS.

2 | Experimental Section

2.1 | Materials

Tetrachloroauric(III) acid trihydrate ($HAuCl_4 \cdot 3H_2O$, Sigma–Aldrich, 99.995 %), acetoacetoxy ethyl methacrylate (AAEM, Sigma–Aldrich, 95 %), acrylic acid (AAc, Sigma–Aldrich, 99%), 3,9-Divinyl-2,4,8,10-tetraoxaspiro[5.5]undecane (VOU, Sigma–Aldrich, 98%), 2,2'-Azobis[N-(2-carboxyethyl)-2-methylpropionamidine] n-Hydrate (ACMA, FUJIFILM Wako Pur Chemical Corporation, 95%), sodium dodecyl sulfate (SDS, Sigma–Aldrich, p.a.), sodium borohydride ($NaBH_4$, Merck, 99%), potassium thiocyanate (KSCN, Fisher Scientific, 98%), cetyltrimethylammonium chloride (CTAC, Sigma–Aldrich, 25 wt.% in H_2O), L(+)-ascorbic acid (AA, Roth, 99%) and phosphate buffer solution (PBS buffer, pH7, Pan React AppliChem) were used as received. *N*-isopropylacrylamide (NIPAM, TCI, 98%) was recrystallized from cyclohexane. Water used for all syntheses and measurements was purified with a MilliQ system (Millipore). The final resistivity of the water was 18 MΩ cm.

2.2 | Synthesis

2.2.1 | Synthesis of Microgels

Microgels were prepared by precipitation polymerization. We present an overview of the chemical structures of all monomers, the crosslinker, and the initiator that were used for the synthesis of the PNIPAM-based copolymer microgels in Scheme S1. All batches were synthesized in a total volume of 50 mL using 100 mL three-necked flasks equipped with a reflux condenser, dropping funnel, and gas inlet. NIPAM (507 mg, 4.48 mmol), stabilizer SDS (6.6 mg, 0.023 mmol), crosslinker VOU (26.7 mg, 0.125 mmol, 2.8 mol%), and comonomer AAEM (112.6 mg, 0.5259

mmol, 11.7 mol%) were dissolved in 40 mL of water under stirring and heating to 70°C. The solutions were purged with nitrogen for at least 30 min. During that time, the zwitterionic initiator ACMA (23.3 mg, 0.0563 mmol) was dissolved in 5 mL of water. After heating, the initiator solution was added. Depending on the synthesis, solutions of 40.35 mg (0.56 mmol, 12.5 mol%), 8.07 mg (0.112 mmol, 2.5 mol%) or 1.61 mg (0.224 mmol, 0.5 mol%) acrylic acid were prepared in water. Ten minutes after the start of the reaction, which was observed by the reaction mixture becoming turbid, the respective solution of acrylic acid in water was added dropwise using a dropping funnel. After 4 h, the dispersion was cooled to room temperature and purified by extensive dialysis against water for one week. After dialysis, we freeze-dried all synthesized microgels.

Precipitation copolymerization with other monomer/comonomer ratios was performed analogue to the protocol described before. The masses and abbreviations for all microgels are summarized in Table 1.

2.2.2 | In Situ Growth of Gold Nanoparticles

For the in situ synthesis, 562 µL of an aqueous microgel dispersion with a concentration of 1 wt.% was transferred into a 4 mL screw top vial. 10 µL of tetrachloroauric(III) acid trihydrate ($HAuCl_4 \cdot 3H_2O$) solution (0.01 M) was added. After stirring for 60 min at room temperature, the reduction of gold was initiated by the addition of 1.5 mL of a freshly-prepared, cold, aqueous $NaBH_4$ solution (0.02 M). The dispersion was then allowed to stir for an additional 90 min. The course of the reaction could be followed visually due to the spontaneous change in color. Right after the addition of $NaBH_4$, the dispersion turned from yellow to pink to a light grey. After a brief period, the formation of black aggregates became visible by the naked eye. These aggregates either rapidly settled at the bottom of the vial or accumulated in the foam at the top of the dispersion. Despite this aggregation—happening potentially outside the microgels—the final dispersion showed a pinkish color. We performed additional experiments where we changed the gold ion concentration by using 50 or 100 mL as compared to 10 mL of the tetrachloroauric(III) acid trihydrate ($HAuCl_4 \cdot 3H_2O$) solution (0.01 M). Purification of the hybrid microgels was performed in a two-step process. First excess gold that formed during the synthesis was removed by short cycles of centrifugation. Hybrid microgels were centrifuged five times for 45 s at 5600 rcf. After each cycle, a black sediment could be identified at the bottom of the tube, which can be attributed to excess gold. The dispersion of hybrid microgels was separated, and the process was repeated. Afterwards, the microgels were centrifuged five times for 20 min at 5600 rcf. After centrifugation, the hybrid microgels were dialyzed against water for one week and finally freeze-dried.

2.2.3 | One-Step Overgrowth of the Gold Cores

For the surfactant-supported overgrowth of the AuNP cores, a modified version of the protocol by Honold et al. was used [60]. First, a feed solution was prepared by adding 112 µL $HAuCl_4$ solution (0.130 M) and 184 µL cetyltrimethylammonium chloride

TABLE 1 | Summary of the synthesis details for all synthesized microgels.

Microgel	*m(NIPAM) [mg] [mmol]*	*m(AAEM) [mg] [mmol]*	*m(AAc) [mg] [mmol]*	*m(VOU) [mg] [mmol]*	*m(SDS) [mg] [mmol]*	*M[ACMA] [mg] [mmol]*
PNIPAM	507 (4.48)	—	—	26.7 (0.125)	6.6 (0.023)	23.3 (0.056)
P(NIPAM-co-$AAc_{12.5\%}$)	507 (4.48)	—	40.35 (0.56)	26.7 (0.125)	6.6 (0.023)	23.3 (0.056)
P(NIPAM-co-AAEM)	507 (4.48)	112.6 (0.526)	—	26.7 (0.125)	6.6 (0.023)	23.3 (0.056)
P(NIPAM-co-AAEM-co-$AAc_{2.5\%}$)	507 (4.48)	112.6 (0.526)	8.07 (0.112)	26.7 (0.125)	6.6 (0.023)	23.3 (0.056)
P(NIPAM-co-AAEM-co-$AAc_{12.5\%}$)	507 (4.48)	112.6 (0.526)	40.35 (0.56)	26.7 (0.125)	6.6 (0.023)	23.3 (0.056)
P(NIPAM-co-AAEM-co-$AAc_{0.5\%}$)	507 (4.48)	112.6 (0.526)	1.61 (0.224)	26.7 (0.125)	6.6 (0.023)	23.3 (0.056)

(CTAC) solution (0.78 M) to 29 mL of water. Next, 200 µL of the hybrid microgel dispersion (2 wt.%) was combined with 200 µL CTAC solution (0.1 M) to create a precursor stock solution. Under heavy stirring, 200 µL of the precursor stock solution, 25.4 µL CTAC solution (0.78 M), and 388 µL of an ascorbic acid (AA) solution (0.049 M) were successively added to 7.975 mL of water in a 100 mL glass vial. The prepared seed solution was combined with the feed solution and stirred for twenty minutes at room temperature. Within the first minutes of the reaction, a shift in color of the dispersion from light pink to orange-brown could be observed. The resulting particles were centrifuged five times for 10 min at 5600 rcf and freeze-dried afterwards.

Alternatively, a surfactant-free approach was tested for AuNP overgrowth. First, 15 µL of a KSCN solution (1 M) was added into a 4 mL screw top vial. Upon addition of 50 µL of solution $HAuCl_4$ (0.05 M) under heavy stirring, the formation of an orange solid was observed. Next, 1.6 mL of phosphate-buffer (pH 7) was transferred to the reaction solution, leading to a spontaneous discoloration. Finally, 1 mL of the hybrid microgel dispersion (1 wt.%) was added to the solution and stirred for 24 h at room temperature. During the progress of the reaction, a slow shift of the color from initially light pink to a deep red was observed.

After the growth process the purification of the obtained microgels was realized by sequential steps of repeated centrifugations. Initially, large gold particles and aggregates that formed outside of the microgels were removed by short centrifugation cycles. The dispersion was centrifuged five times at 5600 rcf for 15 s each. After each cycle, the black sediment was removed prior to the next cycle of centrifugation. At these short times of centrifugation, the larger fraction of the hybrid microgels remained stable in dispersion in the supernatant. Then, the hybrid microgels were centrifuged five times for 50 s at 5600 rcf. After each step, the supernatant was removed and the residue containing the microgels was redispersed in water. Finally, the microgels were dialyzed against water for one week and freeze dried afterwards.

3 | Methods

3.1 | Transmission Electron Microscopy (TEM)

TEM was performed on a JEOL JEM-2100Plus operating in bright-field mode at 80 kV acceleration voltage. Samples were prepared by drop-casting 7 µL of dilute microgel dispersions on carbon-coated copper grids (200 mesh, Science Services). The radii of the microgels were obtained using the image analysis software ImageJ.

3.2 | UV–vis Absorbance Spectroscopy

Absorbance spectra were recorded using a Specord S600 (Analytic Jena AG) spectrophotometer. The spectrometer was equipped with an eightfold cuvette holder and a Peltier element for precise temperature control with an accuracy of ± 0.1°C. The sample temperature was monitored using a cuvette with a temperature probe immersed in water. The microgel dispersions with solid contents of 0.02 wt.% in water were measured in PMMA cuvettes with a light path of $d = 1$ cm. For every measurement, a reference spectrum in water was recorded and subtracted. Measurements were performed in the wavelength range of 182 to 1019 nm at temperatures between 5°C and 55°C in steps of 1°C. At each temperature, the samples were equilibrated for 10 min before the respective measurement. Additionally, singular measurements were performed at 20°C using the same measurement conditions.

3.3 | Electrophoretic Light Scattering (ELS)

Electrophoretic mobilities were determined using a Zetasizer Nano ZS (Malvern Panalytical). Aqueous microgel dispersions were diluted to 0.02 wt.% and measured in folded capillary cells (DTS 1070, Malvern Panalytical). For all samples, we performed measurements at 20°C and 50°C with equilibration times of 600 s. Each measurement was repeated three times.

3.4 | Dynamic Light Scattering (DLS)

Hydrodynamic radii, R_h were determined by DLS using a Zetasizer Nano S (Malvern Panalytical). The device detects scattered light at a scattering angle of 173°. We performed singular measurements at 20°C and 50°C and measurements in a temperature range of 15°C and 55°C in steps of 1°C with a thermal stability of ± 0.1°C. The samples were equilibrated for 10 min at each temperature before the respective measurement. We performed three measurements with an acquisition time of 60 s for each temperature. All samples were diluted to a concentration of 0.02 wt.% using MilliQ water. The pH was not adjusted. Therefore, all samples should be in the range of pH of 5 to 7, that is, in a range where the AAc (if used as comonomer) is in its deprotonated state. Samples were measured in semimicro PMMA cuvettes. The error bars used within this work correspond to the standard deviation of the hydrodynamic radii. The dispersity is an indication of the overall distribution of the determined size, assuming a single mean, and is calculated by cumulant analysis performed by the Malvern Panalytical measurement software.

3.5 | Small-Angle X-Ray Scattering (SAXS)

SAXS measurements were performed on a Xeuss 2.0 (XENOCS) equipped with an X-ray source that provides a beam with an energy of 8.048 keV. The sample-to-detector distances were set to 0.55 and 2.495 m, and measurements were performed with acquisition times of 900 and 1800 s, respectively. Scattering patterns were recorded with a Pilatus3R 300 K detector providing an area of 83.8 × 106.5 mm^2 and a pixel size of 172 × 172 μm^2. In this case, the setup provides a q-range of 0.03 $nm^{-1} < q < 5$ nm^{-1}. Scattering profiles for both sample-to-detector distances were merged in the q-range between 0.1 and 0.25 nm^{-1}. Dilute samples were measured in 1 mm round capillaries (WJM Glas) at a temperature of 20°C. The measured signal was background-corrected for the scattering of water and then radially averaged with the Foxtrot software provided by Xenocs. Fitting of the scattering profiles was conducted with the SasView software [61].

3.6 | Nuclear Magnetic Resonance (NMR) Spectroscopy

^{1}H-spectra were measured at 298 K on an Avance NEO evo 600 from Bruker. Samples were measured in dimethyl sulfoxide-d_6, leading to a signal with a chemical shift at ^{1}H δ 3.33 ppm.

4 | Results and Discussion

By performing precipitation polymerizations of NIPAM with the crosslinker VOU and the zwitterionic initiator ACMA, both in the absence and presence of AAc as a chargeable co-monomer, we successfully synthesized PNIPAM and P(NIPAM-co-AAc$_{12.5\%}$) copolymer microgels. These will serve as the starting point for the investigation of the in situ reduction for the formation of AuNPs.

Monodisperse microgels that show the typical VPT behavior were successfully obtained in both cases, as revealed by TEM imaging and temperature-dependent DLS measurements shown in Figure 1. Figure 1a,c shows swelling curves as obtained from DLS measurements. The continuous reduction of the hydrodynamic radii with increasing temperature in the vicinity of the VPT temperature shows the expected sigmoidal trends for thermoresponsive microgels. The Boltzmann fits to the data (red solid lines) yield VPT temperatures (VPTTs) of 27.2°C and 27.9°C, respectively. The microgels exhibit hydrodynamic radii of 78 ± 1 nm and 112 ± 2 nm in the swollen state at 20°C and 56 ± 1 nm and 87 ± 1 nm in the collapsed state at 50°C for PNIPAM and P(NIPAM-co-AAc$_{12.5\%}$) microgels, respectively. Compared to "classical" PNIPAM microgels that are typically synthesized with *N*,*N*'-methylenebisacrylamide (BIS) as chemical crosslinker and with anionic radical initiators like potassium or ammonium persulfate [4, 62, 63], our PNIPAM microgels are relatively small and possess a lower VPTT. The smaller size can be attributed mostly to the SDS used in the present synthesis [64]. The lower VPTT as compared to the typical values of 32°C–34°C for "classical" PNIPAM microgels, is related to the more hydrophobic character of VOU as compared to BIS. It is known from literature that introducing hydrophobic moieties into PNIPAM-based microgels leads to a reduction of the VPTT [65]. The fact that our P(NIPAM-co-AAc$_{12.5\%}$) copolymer microgels are larger than the PNIPAM microgels, both in the swollen and collapsed state, points to the additional ionic contribution to the osmotic pressure due to the introduction of the carboxy groups. This leads to stronger swelling of the microgels, increasing their hydrodynamic dimensions [66]. The effect on the VPTT however, is minor as compared to the PNIPAM microgels. A two-step phase transition as reported in literature for P(NIPAM-co-AAc) microgels with high charge densities is not observed [66]. This might point to a lower degree of incorporation for our microgels, reducing the charge density and/or a more homogeneous distribution of the AAc comonomers throughout the microgel network.

The sizes of the microgels and their narrow size distributions were also confirmed by the TEM. Representative images are shown as insets in Figure 1 next to the swelling curves. The successful incorporation of acrylic acid into the microgels was confirmed by electrophoretic light scattering (ELS) measurements. These measurements revealed a zeta potential of -38 mV for the P(NIPAM-co-AAc$_{12.5\%}$) microgels as compared to +1 mV (basically zero) that was measured for the PNIPAM microgels without AAc. In Figure 1b,d, representative TEM images of the microgels after the in situ reduction to form AuNPs are shown. As suggested by the TEM images prior to purification, in both cases, a large number of AuNPs formed outside the microgels, resulting in aggregates with uncontrolled shapes and sizes. These aggregates show a strong contrast in the TEM images compared to the microgels due to the much higher electron density. Notably, no evidence of NP formation within the microgels was observed. We will now turn to copolymer microgels that contain AAEM as a functional comonomer. This is motivated by the earlier work of Thies et al. where the β-diketone groups were found crucial to the formation of AuNPs within poly(*N*-vinylcaprolactam) (PVCL) microgels [57].

4.1 | Role of β-diketone Groups for the Formation of AuNPs

Compared to the previously discussed microgels, the obtained P(NIPAM-co-AAEM) microgels exhibit a hydrodynamic radius R_h of 179 ± 5 nm in the swollen state at 20°C and show lower colloidal stability, as evidenced by the abrupt increase in hydrodynamic radius above 33°C (Figure 2a). This aggregation was found to be reversible, and the aggregates disappeared upon cooling. This behavior is evidence for the missing electrostatic stabilization and attractive interactions that become relevant as the microgels collapse and lose their steric stabilization. Indeed, similar to the PNIPAM microgels, a zeta potential close to zero was measured (-2 mV). Due to the aggregation, we cannot determine the VPTT as we do not know the individual microgel size in the fully collapsed state. Despite the weak colloidal stability, we performed in situ reduction experiments with the P(NIPAM-co-AAEM) microgels at room temperature, which is below the temperature where the microgels start to aggregate. Figure 2b,c shows digital photographs of the microgels prior and after the in situ synthesis. A typical turbid dispersion can be identified prior to the in situ synthesis, which is expected for microgel and latex dispersions due to the scattering of light [67–69].

For the P(NIPAM-co-AAEM) microgels, we performed the in situ synthesis using three different concentrations of $HAuCl_4$ while keeping the microgels concentration constant. In the TEM image presented in **(c)**, we used 50 µL (0.01 M) of $HAuCl_4$. This image shows purified microgels with AuNPs present in some of the microgels. Albeit the small number of microgels shown, we see a rather uncontrolled distribution of AuNPs, with 'empty' microgels and others containing one or more AuNPs that seem to be located in the microgel periphery rather than the center.

Using lower concentrations of $HAuCl_4$ during the synthesis increased the number of empty microgels, although multiple AuNPs occasionally formed within a few microgels. Conversely, higher concentrations of $HAuCl_4$ led to fewer unloaded microgels but resulted in the formation of multiple AuNPs, up to ten per microgel in certain instances. Exemplary TEM images for all three concentrations of $HAuCl_4$ used in the reduction are provided in Figure S1. For all three concentrations of $HAuCl_4$, the size D_{TEM} of formed NPs was determined in a range between 8 ± 2 nm for the lowest concentration and 7 ± 2 nm for the highest concentration. Thus, the size of the formed AuNPs

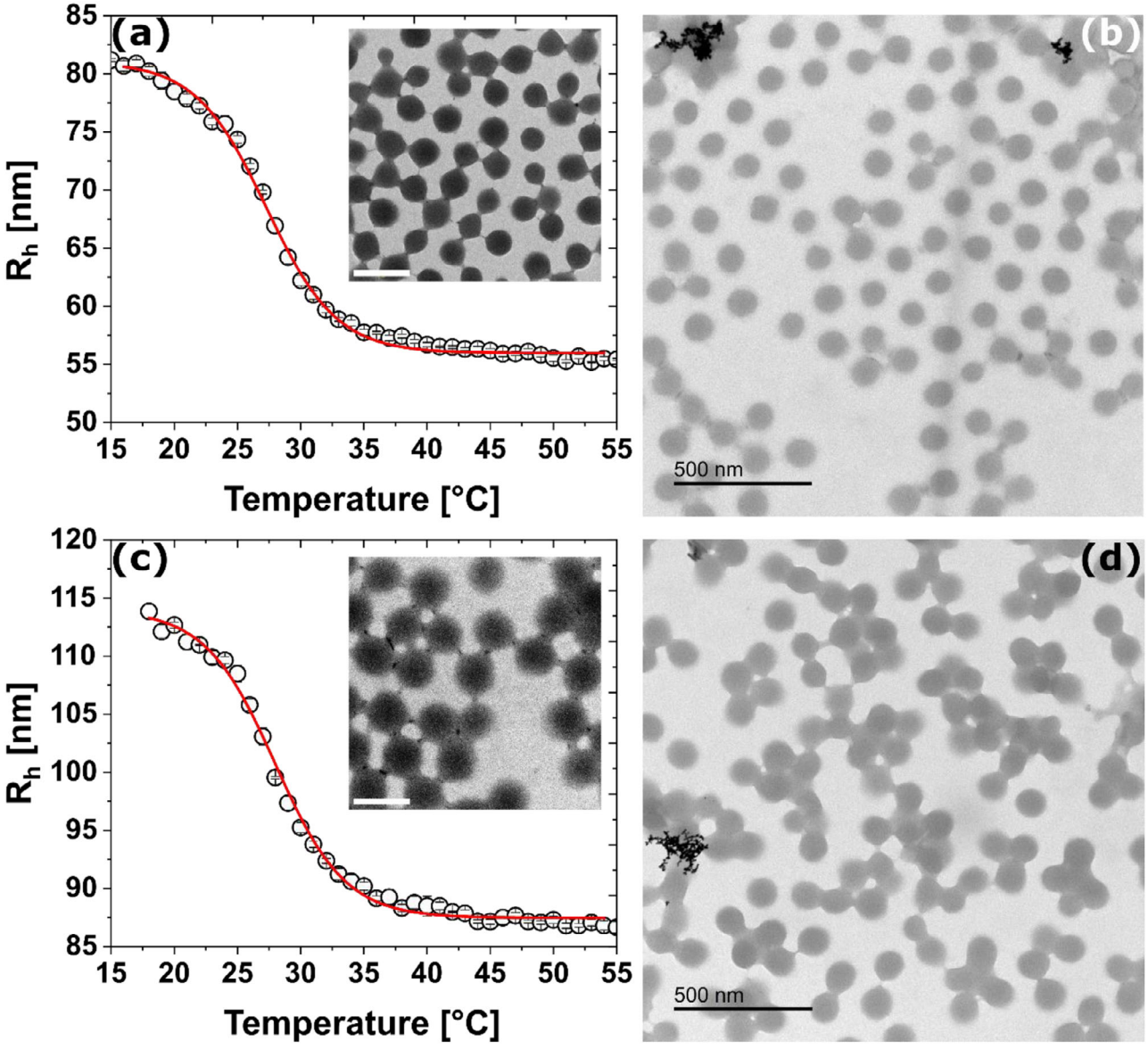

FIGURE 1 | Hydrodynamic radii of (a) PNIPAM and (c) P(NIPAM-co-$AAc_{12.5\%}$) copolymer microgels in dependence of temperature as determined by DLS. The solid red lines correspond to Boltzmann fits to the data. The insets show representative TEM images of the respective microgels. The scale bars in the insets correspond to 200 nm. Exemplary TEM images after the in situ synthesis of AuNPs prior to purification for (b) "classical" PNIPAM microgels and (d) P(NIPAM-co-$AAc_{12.5\%}$) copolymer microgels.

appears to be unaffected by the concentration of $HAuCl_4$ for these P(NIPAM-co-AAEM) microgels.

The inconsistent and uncontrolled loading of the microgels is also reflected in the color change of the microgel dispersion after the in situ formation and purification. The microgel dispersion presented in the digital photograph in Figure 2d shows a slight change from initially colorless to barely perceptible pink. The weak coloring suggests that the majority of the microgels do not contain AuNPs.

Regardless of the ratio of gold ions to microgels and the reaction conditions, we were unable to achieve an in situ synthesis where each microgel contains only a single AuNP. This observation may be related to inhomogeneities in the internal structure of the microgels. We assume that the formation of AuNPs can only occur in AAEM-rich domains, which presumably favor and cause the accumulation of gold ions in these regions of the microgels.

Surprisingly, we found that after the in situ synthesis with P(NIPAM-co-AAEM) microgels, previously unstable, exhibit colloidal stability and could be heated above the VPTT without aggregation, despite showing only a slightly more negative zetapotential of -9 mV in the swollen state at 20°C (Figure S2). The increase in colloidal stability might be caused by structural or chemical changes during the in situ process.

Through our experiments, we identified AAEM as a crucial functionality for in situ synthesis. To further investigate its role, we conducted experiments in which we added only the AAEM monomer to an $HAuCl_4$ solution and stirred the mixture for one week. The amounts of AAEM and $HAuCl_4$ were adjusted

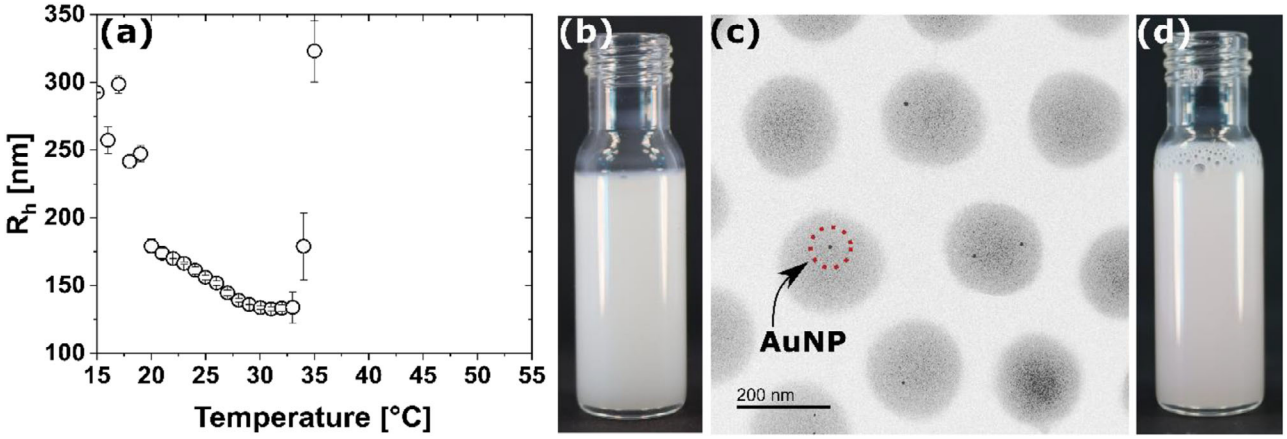

FIGURE 2 | (a) Hydrodynamic radius of P(NIPAM-co-AAEM) microgels in dependence of temperature as determined by DLS. (b) Digital photograph of the initial microgel dispersion prior to the in situ synthesis. (c) Exemplary TEM image of P(NIPAM-co-AAEM) after in situ synthesis, with one AuNP marked with a red circle for clarification. (d) Digital photograph of the microgel dispersion after the in situ synthesis.

to match those used in the in situ experiments presented in this work. Prior to the experiments, AAEM was purified via alumina column chromatography to remove inhibitors, and all reactions were conducted in the dark to eliminate potential light-induced effects. Surprisingly, we found that the presence of AAEM monomer alone led to the formation of a colloidally stable dispersion of AuNPs. Our findings suggest that AAEM not only facilitates the complexation [70] and reduction of gold ions [71] but also enhances the colloidal stability of the formed AuNPs. The results of this experiment are presented in Figure S3.

To increase colloidal stability by electrostatic repulsion, in the next step, we added AAc as an ionizable monomer during the synthesis of the microgel.

4.2 | Role of Carboxylic Acid Groups for the Formation of AuNPs

We start with P(NIPAM-co-AAEM-co-$AAc_{2.5\%}$) microgels that were synthesized with a nominal AAc content of 2.5 mol%. The obtained microgels have a hydrodynamic radius R_h of 156 ± 2 nm in the swollen state at 20°C. Compared to the P(NIPAM-co-AAEM) microgels, these more complex microgels show colloidal stability at higher temperatures due to the additional electrostatic stabilization resulting from the negatively charged carboxylic acid groups at neutral pH. The increased charge is confirmed by the obtained zeta potential of -39 mV (20°C). Using temperature-dependent DLS measurements, shown in Figure 3a, we determined the VPTT of the microgels at 27.7°C.

In Figure 3b, we show a TEM image of the microgels after the successful in situ reduction. The image verifies the successful formation of single AuNPs with a size D_{TEM} = 10 ± 1 nm in each individual microgel. The digital photograph of the hybrid microgel dispersion shown in Figure 3c shows the typical turbid appearance with a pinkish color related to the LSPR of the AuNP cores [69]. Our findings suggest that the incorporation of AAc is essential for the controlled in situ synthesis of AuNPs.

Similar to our findings for the P(NIPAM-co-AAEM) microgels, we observed a change in the swelling properties of the microgels after the in situ reduction process. The VPTT of the hybrid microgels is shifted toward higher temperatures to 36.2°C, and an increase in size by nearly 80 nm at 20°C can be observed. While these changes might be related to the presence of the small AuNPs and their charge density, providing an additional ionic contribution to the osmotic pressure, we believe that it is more likely that the β-diketone groups of the AAEM undergo a chemical reaction during the in situ reduction that employs $NaBH_4$ as a reducing agent. It is possible that the ketones are reduced to secondary alcohols.

To further investigate the role of AAc, we synthesized two microgels with nominal AAc contents of 12.5 and 0.5 mol%. For microgels with 12.5 mol% AAc, we did not find a noticeable difference in the properties of the hybrid microgels and AuNPs before and after the in situ synthesis. Despite the fivefold increase in the AAc feeding concentration compared to P(NIPAM-co-AAEM-co-$AAc_{2.5\%}$), the P(NIPAM-co-AAEM-co-$AAc_{12.5\%}$) microgels possess a nearly identical hydrodynamic radius R_h of 154 ± 1 nm at 20°C and a VPTT of 25.1°C (Figure S4). After the in situ synthesis, the size increased to 196 ± 4 nm with a VPTT of 36.5°C. Additionally, the size D_{TEM} of the AuNPs was determined as 9 ± 1 nm, matching the sizes we found for the P(NIPAM-co-AAEM-co-$AAc_{2.5\%}$) microgels.

For microgels with 0.5 mol% nominal AAc content, TEM images after the in situ synthesis resemble basically our results for the P(NIPAM-co-AAEM) microgels. At such low AAc contents, the in situ reduction led to only a few microgels containing AuNP cores (Figure S5). These experiments reveal that a certain charge density seems to be needed for the controlled formation of single AuNPs in each microgel.

With the aim to validate the complexation and potential localization of gold ions within the β-diketone-containing microgels, we centrifuged a microgel dispersion after the initial addition of $HAuCl_4$ and subsequent stirring for 60 min. After each cycle of centrifugation, we removed the supernatant and redispersed the microgels in water. By repeating the process ten times, we ensured that non-complexed gold ions were completely removed from the supernatant, leaving only ions accumulated inside of

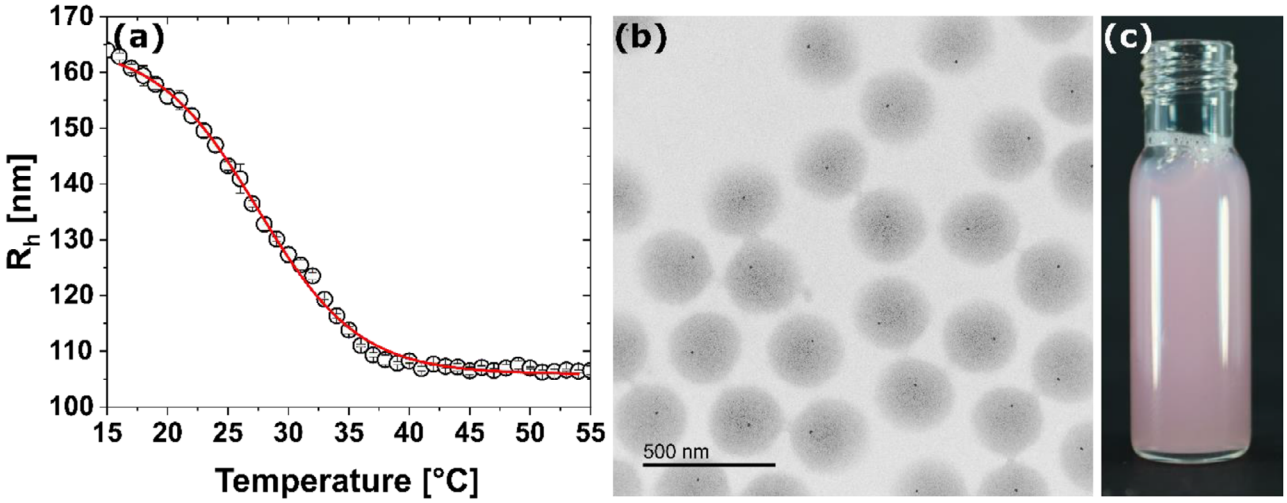

FIGURE 3 | (a) Temperature-dependent evolution of the hydrodynamic radius of P(NIPAM-co-AAEM-co-$AAc_{2.5\%}$) microgels from DLS. The solid red line represents a Boltzmann fit to the data. (b) Exemplary TEM image after the in situ synthesis and purification of P(NIPAM-co-AAEM-co-$AAc_{2.5\%}$) microgels, showing single AuNPs within each microgel. (c) Digital photograph of the corresponding microgel dispersion.

the microgels. After the separation, the remaining gold ions were reduced by the addition of $NaBH_4$. In Figure S6, we present exemplary TEM images that show the resulting microgels after this step of reduction. The images confirm the formation of single AuNPs within the microgels. This experiment suggests that i) the diketone functionalities indeed lead to complexation of the gold ions, and ii) the diketone functionalities are located rather in the central region of the microgels, similar to the findings in the work of Thies et al. [57]. To further support this hypothesis, we conducted an experiment in which $NaBH_4$ was added already 60 s after the addition of $HAuCl_4$ to the microgels. The recorded TEM images reveal that only a few microgels contain formed AuNPs (Figure S7). The short time frame before the reduction seems insufficient to accumulate enough gold ions within the microgels.

Similar to our experiments with the P(NIPAM-co-AAEM) microgels, we compare the results after the in situ synthesis and purification for three different concentrations of $HAuCl_4$ in Figure 4 to get a deeper understanding of the influence of the ratio of gold ions to microgels. In **(a)**—**(c)**, we present schematics and the corresponding TEM images of in situ syntheses performed with P(NIPAM-co-AAEM-co-$AAc_{2.5\%}$) microgels using amounts of 10, 50, and 100 µL (0.01 M) of $HAuCl_4$. The results for the synthesis presented in **(a)** are almost identical to those that we presented in Figure 3b, emphasizing on the reproducibility of the synthesis. In contrast to our observations in **(a)**, in **(b)**, using five times the amount of $HAuCl_4$ led to a 40 % increase in the size of the AuNPs to 14 ± 4 nm. TEM imaging reveals that the increase in size is partially caused by the formation of two NPs that appear to be similar in size and are located very close to each other, seemingly growing together during the in situ process. We cannot confirm whether the increase in size is only related to the aggregation of individual AuNPs or also to the successive growth of initial, single AuNPs. Occasionally, we can observe the formation of an isolated second NP, which occurs in less than 5% of the microgels. In **(c)**, further doubling the amount of $HAuCl_4$ did not further increase the size of the AuNPs (D_{TEM} of 13 ± 4 nm) but led to the formation of two or more AuNPs per microgel.

Our observations for the P(NIPAM-co-AAEM-co-$AAc_{2.5\%}$) microgels differ from the results that we found for the P(NIPAM-co-AAEM) ones. Obviously, there is a cooperative effect of both comonomers, the AAEM and the AAc. The incorporation of both monomers leads to the formation of a catalytically active microgel system, which consequently enables the controlled synthesis of AuNPs. To fully understand the role of different functionalities and their distribution and local density in the microgels, further experiments will be needed in the future, potentially involving neutron scattering with contrast variation and/or super-resolution microscopy with selective labeling.

We now want to address the changes to the microgel swelling behavior upon the in situ formation of AuNP cores. In a recent work, we have shown that correlating the normalized absolute change in sample turbidity to the normalized absolute change in microgel size can be useful to indicate potential heterogeneities in copolymer microgels [68]. For classical PNIPAM microgels crosslinked with *N*,*N*'-methylenebisacrylamide (BIS), we observed a linear correlation between the normalized turbidity (indirectly reflected by the absorbance) and the normalized change in hydrodynamic size in our previous work [72]. This dependence results from the transition of fuzzy spheres with a loose corona in the swollen state to homogeneous spheres in the collapsed state [69]. In the presence of internal heterogeneities, these will contribute differently to the change in turbidity that is sensitive to the refractive index and object size as compared to the hydrodynamic size from DLS which is only determined by the diffusion coefficient in dispersion. As Figure S8 shows, we also observe a quite good agreement to the linear trend for our PNIPAM microgels that are crosslinked with VOU. This suggests that the internal structure is somewhat comparable to PNIPAM microgels crosslinked with BIS. Small-angle scattering (neutrons or X-rays) would be needed to further confirm that indeed the VOU-crosslinked PNIPAM microgels possess the typical fuzzy sphere structure in the swollen state. This is beyond the scope of the present work, and we rather want to focus on the qualitative changes when analyzing the P(NIPAM-co-AAEM-co-$AAc_{2.5\%}$) prior (Figure 5a,b) and after the in situ synthesis for AuNPs (Figure 5c,d). In Figure 5a we see that

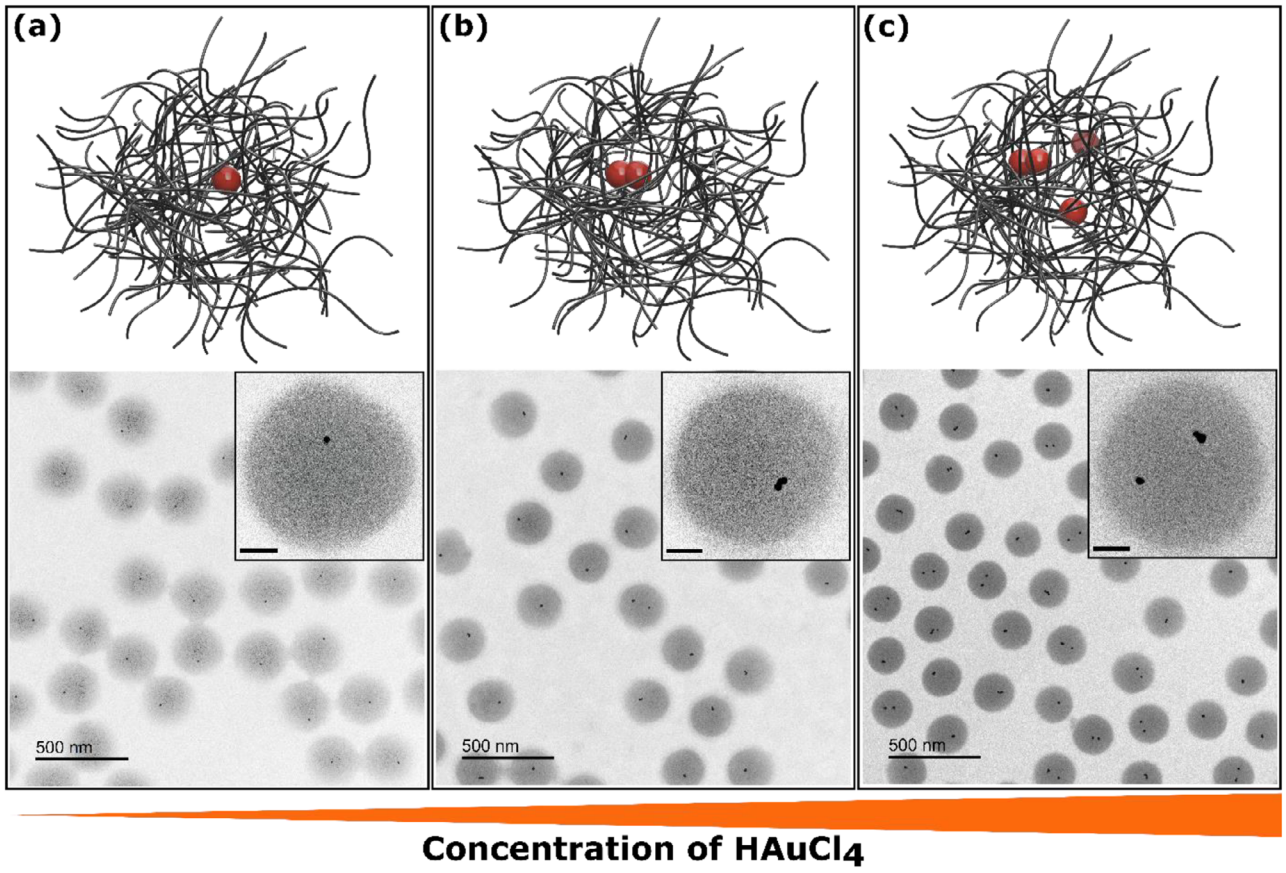

FIGURE 4 | Schematic illustration and corresponding TEM images for in situ experiments with P(NIPAM-co-AAEM-co-$AAc_{2.5\%}$) microgels using different concentrations of $HAuCl_4$. The concentration increases from left to right. The amounts used are: (a) 10 μL, (b) 50 μL, and (c) 100 μL of a 0.01 M $HAuCl_4$ with 562 μL of a 1 wt.% microgel dispersion. The insets show TEM images of single microgels at higher magnifications. The scale bars in the insets correspond to 50 nm.

the normalized profiles from turbidity (change in absorbance) and from DLS (change in R_h) do not match. The transition temperature in the turbidity profile is significantly shifted toward smaller temperatures. The mismatch between both normalized profiles leads to the deviation from the linear trend when correlating both datasets as shown in Figure 5b. Interestingly, a strong change is observed for the purified microgels after the in situ reduction that was used to form AuNPs inside the microgels. The transition temperature seen from the turbidity profile is now shifted to significantly larger values as compared to the swelling curve based on R_h determined from DLS (Figure 5c). This also leads to a strong deviation from the linear trend when correlating both datasets, as seen in Figure 5d. Here, the data lie below the solid line with a slope of −1. In other words, before the in situ reduction, the turbidity changes stronger at lower temperatures than R_h does. While the turbidity remains nearly constant from 30°C onwards, the radius continues to drop until approximately 35°C. In contrast, after the in situ reduction, the opposite is the case. While we currently have no explanation for this dramatic change, this direct comparison underlines clearly that the in situ reduction leads to changes of functional groups within the microgel network that potentially also induce local structural changes. Also, the data indicate that these copolymer microgels possess local heterogeneities that we relate to the distribution of the comonomers throughout the microgel volume.

Based on our observations regarding the accumulation of gold ions related to the β-diketone groups within the microgels and the subsequent formation of well-defined AuNPs, along with the extensive characterization in this work, we want to conclude with a schematic illustration (Scheme 1). Upon the addition of sodium borohydride, the gold ions, which are accumulated in larger quantities within AAEM-rich domains, are reduced, resulting in the formation of AuNPs that are localized within the copolymer microgels.

Although we did not perform a systematic long-term stability experiment on the newly synthesized CS microgels, several of our DLS and spectroscopy experiments were conducted at different time intervals and in some cases months after the initial synthesis. Based on our observations, we have no indication on aging and/or degradation of the microgels. Both the LSPR and the VPT properties were highly reproducible.

4.3 | In Situ Overgrowth of the AuNP Cores

To enhance the plasmonic properties of the hybrid microgels and to further prove that the in situ synthesized AuNPs are well embedded in the microgels, we used wet-chemical overgrowth of the AuNP cores. We begin with a surfactant-assisted overgrowth protocol adapted from Honold et al., where CTAC was used in

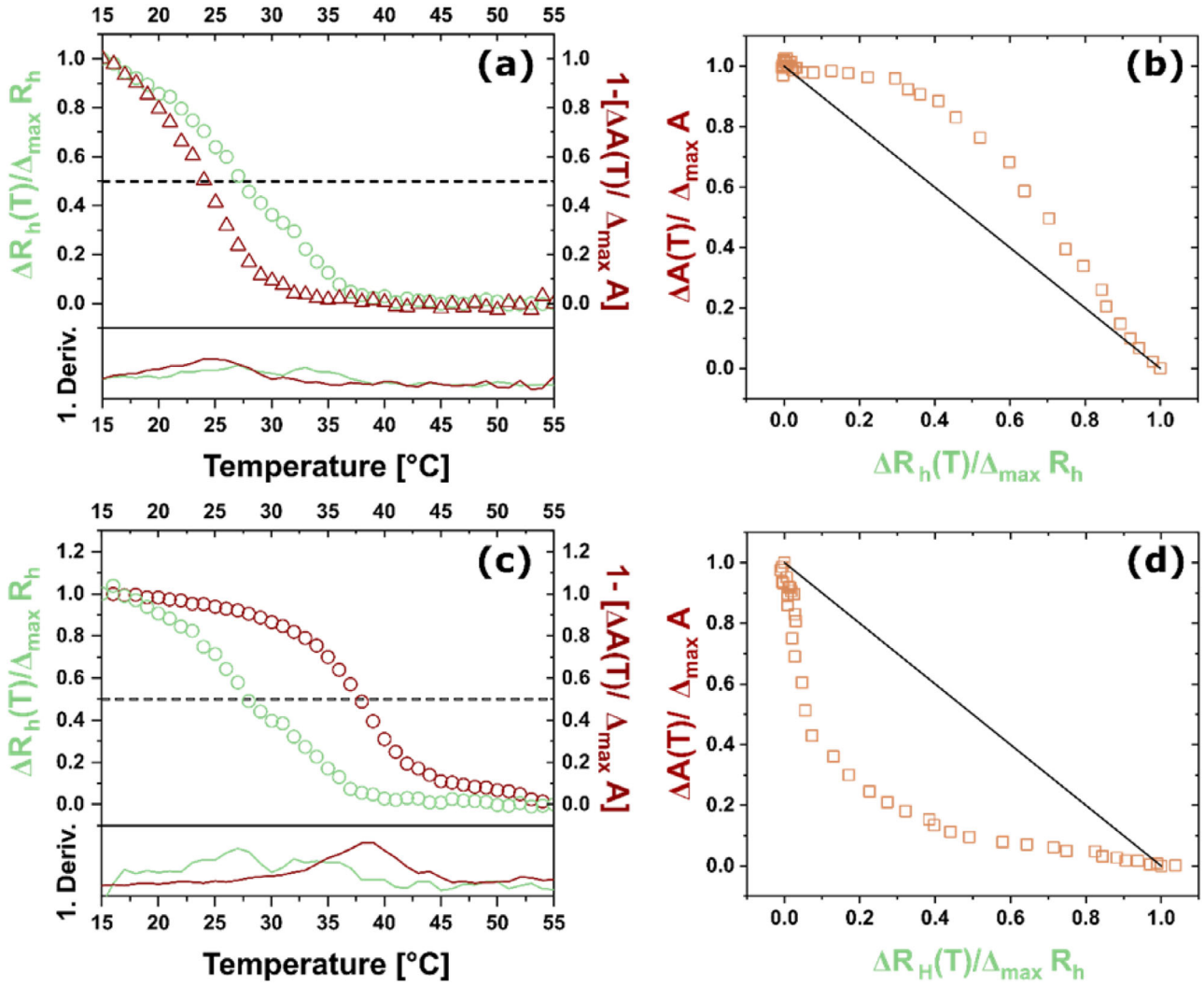

FIGURE 5 | Results from temperature-dependent DLS and absorbance measurements for P(NIPAM-co-AAEM-co-$AAc_{2.5\%}$) microgels prior to (a) and (b) and after in situ synthesis of AuNP cores (c) and (d). (a) and (c) Plots of the normalized change in R_h from DLS in green (left y-axis) and the normalized change in absorbance in red (right y-axis) as a function of temperature. (b) and (d) Plots of the normalized change in absorbance as a function of the normalized change in R_h. The black lines in (b) and (d) are auxiliary lines with a slope of −1.

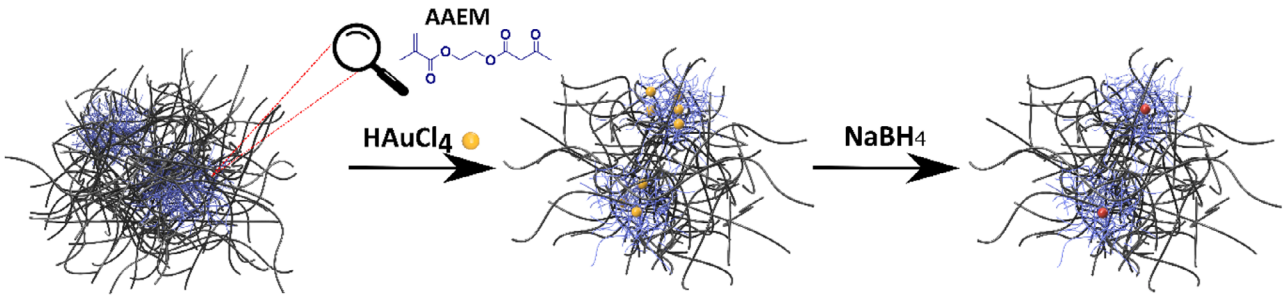

SCHEME 1 | Schematic illustration of the complexation and localization of gold ions inside the copolymer microgels and the following in situ formation of AuNPs inside the microgel network.

the growth of gold cores embedded in PNIPAM microgels [60]. For such overgrowth protocols, it is known that AuNPs in the hybrid copolymer microgels act as catalysts that promote the growth of the individual particles [73–75]. Figure 6 summarizes the results of the overgrowth using the hybrid microgels made from our P(NIPAM-co-AAEM-co-$AAc_{2.5\%}$) microgels. In **(a)**, we present UV–vis absorbance spectra of samples before and after the overgrowth process. The spectrum in pink that corresponds to the initial CS microgels prior to overgrowth, we see the typical power-law decrease in absorbance with increasing wavelength related to light scattering from the PNIPAM microgels. The absorption of the small AuNP cores is too weak to significantly contribute to

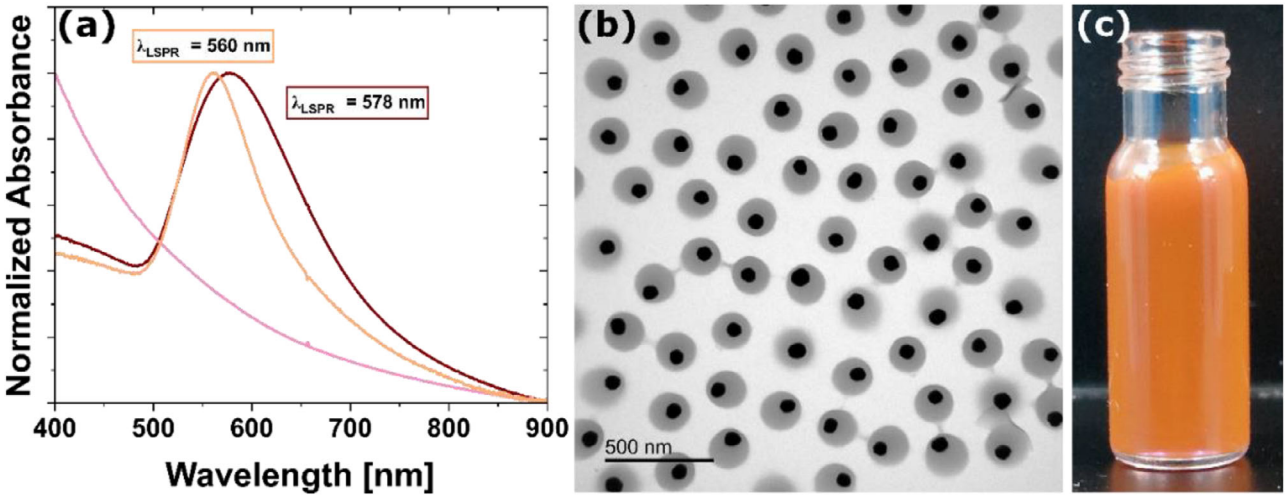

FIGURE 6 | In situ overgrowth of the AuNP cores in P(NIPAM-co-AAEM-co-$AAc_{2.5\%}$) microgels. (a) Absorbance spectra measured from dilute microgel dispersions before (pink) and after the overgrowth process. The spectrum in orange refers to the microgels after surfactant-supported overgrowth, and the one in dark red to surfactant-free overgrowth. (b) Exemplary TEM image of the hybrid microgels after the surfactant-supported overgrowth of the AuNP cores. (c) Digital photograph of the corresponding dilute, aqueous microgel dispersion from (b).

the absorbance of the hybrid microgels [51]. In contrast, hybrid microgels after the surfactant-supported overgrowth show a local maximum at 560 nm, attributed to the more pronounced LSPR of the AuNP cores. The relatively small resonance width (full width at half maximum, FHWM of approximately 140 nm) points to a relatively small size and shape distribution. This assumption is supported by the TEM image shown in **(b)**. The near-spherical cores have an average diameter of D_{TEM} = 76 ± 9 nm. Due to this approximately eightfold increase in diameter, an aqueous dispersion of these hybrid microgels appears with a strong orange coloration with pronounced turbidity as seen in Figure 6c.

We also attempted an overgrowth procedure without surfactant. The obtained hybrid microgels show a significantly broader LSPR peak with a maximum at 578 nm as shown in Figure 6a (spectrum in dark red). While the redshift as compared to the microgels obtained from the CTAC-assisted overgrowth, indicates larger core sizes, the increased FWHM points to a higher dispersity in size and potentially shape. Indeed, representative TEM images presented in the Supporting Information (Figure S9) confirm this assumption. The average core diameter from TEM is 83 ± 13 nm. Despite the larger standard deviation in size, we observe a significantly larger dispersity in shape with some rod- and triangular-shaped AuNPs. This difference with respect to the core uniformity form the CTAC-assisted growth is also reflected by the optical appearance of a dilute, aqueous dispersion that shows a dark red color. While overgrowth is also possible without the use of a surfactant, the CTAC-assisted protocol yields more uniform and near-spherical overgrown cores.

4.4 | Analysis of the form Factor of the AuNP Cores Using SAXS

Apart from statistically limited analysis of the core size and morphology from imaging using TEM, we made use of the strong difference in X-ray scattering contrast of the AuNP cores with respect to the low electron density PNIPAM shells and used SAXS as an ensemble technique to study the form factor of the cores. Figure 7a,b shows the change in the scattering profiles before and after the in situ synthesis using the P(NIPAM-co-AAEM) and P(NIPAM-co-AAEM-co-$AAc_{2.5\%}$) microgels, respectively. In **(a)**, the scattering profile in black corresponds to the P(NIPAM-co-AAEM) microgels prior to the formation of AuNPs, while the blue profile shows the scattering profile after the in situ synthesis with 50 µL of $HAuCl_4$. In both cases, the scattering signal is weak, the profiles show large error bars and visible fluctuations, including some oscillations in intensity are rather related to the weak scattering and therefore poor statistics rather than any form factor. A Porod fit (q^{-4}) to the date (orange solid line) roughly describes the experimental data. This indicates that scattering from the interface of the relatively large microgels compared to the covered q-range of this SAXS experiment is dominating the scattering profile. The profile of the microgels after in situ synthesis of AuNPs in blue shows some increase in scattering in the mid q-range that we attribute to scattering from the high electron density AuNPs. Indeed, a combination (solid red line) of a Porod fit and the polydisperse sphere model (red dashed line) describes the experimental data relatively well. The polydisperse sphere contribution yields an average particle diameter of 9 ± 3 nm which is slightly higher than the diameter of 8 ± 2 nm determined by TEM, but still in very good agreement given the accuracy of the SAXS data. Additional information about the parameters obtained from fits to all scattering profiles can be found in Tables S3–S4.

In Figure 7b we compare SAXS profiles for the P(NIPAM-co-AAEM-co-$AAc_{2.5\%}$) microgels prior to and after the in situ synthesis of AuNPs. While the noisy profile of the purely organic microgels is quite similar to the one shown in **(a)** for the P(NIPAM-co-AAEM) microgels, the form factor contribution of the AuNP cores is much more prominent in the profile in blue in **(b)** than for the P(NIPAM-co-AAEM) with in situ synthesized AuNPs. Again, a combination of the Porod fit and a polydisperse hard sphere form factor was used to describe the data (red line). The sphere form factor yielded an average particle diameter of

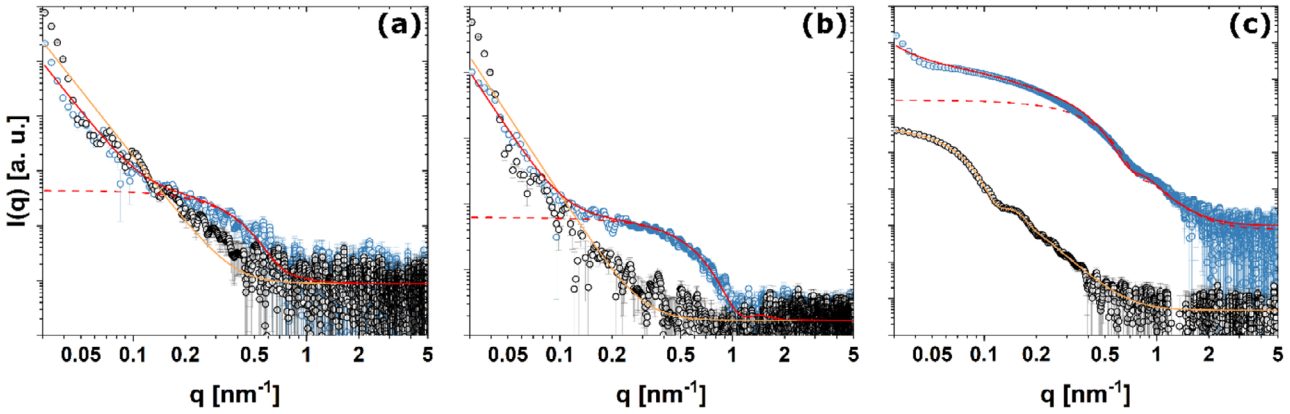

FIGURE 7 | Radially averaged SAXS profiles for different microgels investigated before and after the formation of AuNPs via in situ synthesis and the overgrowth procedure. (a) SAXS profiles before (black) and after (blue) in situ synthesis using P(NIPAM-co-AAEM) microgels with 50 μL $HAuCl_4$. (b) Comparison of scattering profiles prior (black) and after the formation of AuNPs (blue) using P(NIPAM-co-AAEM-co-$AAc_{2.5\%}$) microgels with 10 μL of $HAuCl_4$. (c) Scattering profiles for the P(NIPAM-co-AAEM-co-$AAc_{2.5\%}$) microgels after surfactant-supported overgrowth of the AuNP cores (black) and P(NIPAM-co-AAEM) microgels after in situ synthesis with 100 μL of $HAuCl_4$ (blue). Solid red and orange lines and dashed red lines correspond to different fit functions and models to describe the scattering profiles of the microgels and hybrid systems. The scattering profiles were shifted vertically by fixed multipliers for better visibility/comparison.

7 ± 1 nm. This value is similar, but smaller than the diameter obtained from TEM imaging (10 ± 1. nm). The more pronounced scattering from the AuNP cores is related to the higher yield in single AuNP cores in the P(NIPAM-co-AAEM-co-$AAc_{2.5\%}$) microgels (see Figures 2b and 3c for comparison). In Figure 7c we compare SAXS profiles for P(NIPAM-co-AAEM-co-$AAc_{2.5\%}$) after surfactant-supported overgrowth of the AuNPs presented in black and P(NIPAM-co-AAEM) after in situ synthesis with a higher amount of 100 μL $HAuCl_4$ shown in blue. As previously described, the in situ synthesis with higher amounts of $HAuCl_4$ led to the uncontrolled formation of multiple AuNPs within the microgels, while the surfactant-supported overgrowth allowed for the homogeneous growth of the AuNP cores. The scattering signal for both samples is significantly larger than for the samples studied in **(a)** and **(b),** and the profiles have much better statistics, revealing clear form factor oscillations in the mid and high q-range. For the overgrown AuNP cores in the P(NIPAM-co-AAEM-co-$AAc_{2.5\%}$) microgels (black symbols) the form factor fit with a polydisperse sphere model (orange line) yields an average core diameter of 70 ± 12 nm, which is in good agreement with the obtained value from TEM (76 ± 9 nm). For the P(NIPAM-co-AAEM) microgels after the in situ synthesis with 100 μL $HAuCl_4$ (blue symbols), we used a combination (red solid line) of a Porod fit, a polydisperse sphere model (dashed, red line), and a fractal model. While the Porod function again covers roughly the contribution of the scattering from the relatively large microgels, the fractal model allows us to describe the contribution of multiple (aggregated) AuNP cores within the microgels as seen by the continuous intensity increase in the mid to low q-range (0.06 to 0.3 nm^{-1}). The average diameter of 12 ± 3 nm from the fit with the polydisperse sphere model noticeably differs from the diameter obtained by TEM evaluation, which was determined to be 7 ± 2 nm. The fractal model provided the correlation length, which characterizes the average size of an aggregate of AuNPs within the microgels in the dispersion. Based on a correlation length of 12.4 nm, we report that the majority of the AuNPs formed during the in situ synthesis with higher amounts $HAuCl_4$ in P(NIPAM-co-AAEM) microgels are aggregates of two AuNPs.

5 | Conclusions

In this study, we demonstrated the successful preparation of hybrid microgels containing single plasmonic nanoparticle cores using PNIPAM-based copolymer microgels as smart nanoreactors for the in situ reduction of gold ions. We found that, besides AAEM being crucial as a complexing comonomer, charged monomers such as AAc are important for both the in situ reduction as well as electrostatic stabilization of the microgels and hybrid microgels. By adjusting the microgel-to-gold ion ratio, we achieved partial control over nanoparticle loading. Notably, we identified a concentration regime in which a single nanoparticle was predominantly formed within each microgel. The LSPR properties of the hybrid microgels can be significantly enhanced by in situ overgrowth of the nanoparticle cores, resulting in multifunctional hybrid microgels that combine catalytic, plasmonic, and thermoresponsive properties. The successful overgrowth also underlines that the nanoparticle cores are well embedded within the copolymer microgels. Importantly, the leaking of nanoparticles out from the microgels was not observed. The obtained hybrid microgels showed a pronounced swelling/deswelling behavior in water induced by temperature. Results from dynamic light scattering in direct relation to turbidity data point to local heterogeneities in our copolymer microgels that are related to the distribution of the AAEM comonomers that are relevant to the local accumulation of gold ions prior to their reduction. Future experiments, including temperature-dependent SANS measurements, might be useful to gain a deeper understanding of the internal structure and composition of these complex copolymer microgels. Additionally, further studies using NMR, infrared spectroscopy, or stimulated emission depletion (STED) microscopy experiments with labeled functional groups could provide valuable insights into the role of the AAEM monomer, the charge introduced by AAc, and the mechanism of in situ nanoparticle formation, as well as structural changes in the microgel system during gold ion reduction. Once the in situ mechanism is better understood, the catalytic potential of these copolymer microgels could be extended to the synthesis of other

metal nanoparticles, such as copper or aluminum, which are difficult to obtain via conventional reduction methods in an aqueous environment. Due to differences in redox potentials, these approaches require careful optimization of synthesis parameters, including pH and reduction conditions.

Acknowledgements

The authors acknowledge the DFG and the State of NRW for funding the cryo-TEM (INST 208/749-1 FUGG). The authors thank the DFG for funding within Collaborative Research Center "Functional Microgels and Microgel Systems" (CRC 985). The authors also would like to thank Déborah Feller (HHU Düsseldorf) for assistance with the surfactan*t-supported overgrowth protocol*. This work benefited from the use of the SasView application, originally developed under NSF award DMR-0520547. SasView contains code developed with funding from the European Union's Horizon 2020 research and innovation programme under the SINE2020 project, grant agreement No 654000.

Open access funding enabled and organized by Projekt DEAL.

Conflicts of Interest

The authors declare no conflicts of interest.

Data Availability Statement

The data that support the findings of this study are available from the corresponding author upon reasonable request.

References

1. M. Karg, A. Pich, T. Hellweg, et al., "Nanogels and Microgels: from Model Colloids to Applications, Recent Developments, and Future Trends," *Langmuir* 35 (2019): 6231–6255.

2. F. A. Plamper and W. Richtering, "Functional Microgels and Microgel Systems," *Accounts of Chemical Research* 50 (2017): 131–140.

3. R. Pelton, "Temperature-Sensitive Aqueous Microgels," *Advances in Colloid and Interface Science* 85, no. 1 (2000): 1–33.

4. R. H. Pelton and P. Chibante, "Preparation of Aqueous Latices with N-Isopropylacrylamide," *Colloids and Surfaces* 20, no. 3 (1986): 247–256.

5. W. Richtering, I. I. Potemkin, A. A. Rudov, G. Sellge, and C. Trautwein, "Could Multiresponsive Hollow Shell–Shell Nanocontainers Offer an Improved Strategy for Drug Delivery?," *Nanomedicine Journal* 11, no. 22 (2016): 2879–2883.

6. N. M. B. Smeets and T. Hoare, "Designing Responsive Microgels for Drug Delivery Applications," *Journal of Polymer Science* 51, no. 14 (2013): 3027–3043.

7. K. Uhlig, T. Wegener, J. He, et al., "Patterned Thermoresponsive Microgel Coatings for Noninvasive Processing of Adherent Cells," *Biomacromolecules* 17 (2016): 1110–1116.

8. D. Keskin, O. Mergel, H. C. Van Der Mei, H. J. Busscher, and P. Van Rijn, "Inhibiting Bacterial Adhesion by Mechanically Modulated Microgel Coatings," *Biomacromolecules* 20 (2019): 243–253.

9. A. W. Bridges, N. Singh, K. L. Burns, J. E. Babensee, L. Andrew Lyon, and A. J. García, "Reduced Acute Inflammatory Responses to Microgel Conformal Coatings," *Biomaterials* 29, no. 35 (2008): 4605–4615.

10. V. Sabadasch, M. Dirksen, P. Fandrich, et al., "Pd Nanoparticle-Loaded Smart Microgel-Based Membranes as Reusable Catalysts," *ACS Applied Materials & Interfaces* 14, no. 43 (2022): 49181–49188.

11. M. Dirksen, T. Brändel, S. Großkopf, et al., "UV Cross-Linked Smart Microgel Membranes as Free-Standing Diffusion Barriers and Nanoparticle Bearing Catalytic Films," *RSC Advances* 11 (2021): 22014–22024.

12. T. Honold, K. Volk, A. Rauh, J. P. S. Fitzgerald, and M. Karg, "Tunable Plasmonic Surfaces via Colloid Assembly," *Journal of Materials Chemistry C* 3, no. 43 (2015): 11449–11457.

13. M. B. Müller, C. Kuttner, T. A. F. König, et al., "Plasmonic Library Based on Substrate-Supported Gradiential Plasmonic Arrays," *ACS Nano* 8, no. 9 (2014): 9410–9421.

14. S. A. Maier, M. L. Brongersma, P. G. Kik, S. Meltzer, A. A. G. Requicha, and H. A. Atwater, "Plasmonics-A Route to Nanoscale Optical Devices," *Advanced Materials* 13, no. 19 (2001): 1501–1505.

15. S. G. Romanov, N. Vogel, K. Bley, et al., "Probing Guided Modes in a Monolayer Colloidal Crystal on a Flat Metal Film," *Physical Review B* 86, no. 19 (2012): 195145.

16. B. Ai, Y. Yu, H. Möhwald, G. Zhang, and B. Yang, "Plasmonic Films Based on Colloidal Lithography," *Advances in Colloid and Interface Science* 206 (2014): 5–16.

17. R. Contreras-Cáceres, A. Sánchez-Iglesias, M. Karg, et al., "Encapsulation and Growth of Gold Nanoparticles in Thermoresponsive Microgels," *Advanced Materials* 20 (2008): 1666–1670.

18. M. Mueller, M. Tebbe, D. V. Andreeva, et al., "Large-Area Organization of pNIPAM-Coated Nanostars as SERS Platforms for Polycyclic Aromatic Hydrocarbons Sensing in Gas Phase," *Langmuir* 28, no. 24 (2012): 9168–9173.

19. Y. Lu, P. Spyra, Y. Mei, M. Ballauff, and A. Pich, "Composite Hydrogels: Robust Carriers for Catalytic Nanoparticles," *Macromolecular Chemistry and Physics* 208, no. 3 (2007): 254–261.

20. A. Pich, A. Karak, Y. Lu, A. K. Ghosh, and H.-J. P. Adler, "Tuneable Catalytic Properties of Hybrid Microgels Containing Gold Nanoparticles," *Journal of Nanoscience and Nanotechnology* 6, no. 12 (2006): 3763–3769.

21. T. Brändel, V. Sabadasch, Y. Hannappel, and T. Hellweg, "Improved Smart Microgel Carriers for Catalytic Silver Nanoparticles," *ACS Omega* 4, no. 3 (2019): 4636–4649.

22. V. Sabadasch, L. Wiehemeier, T. Kottke, and T. Hellweg, "Core–Shell Microgels as Thermoresponsive Carriers for Catalytic Palladium Nanoparticles," *Soft Matter* 16, no. 23 (2020): 5422–5430.

23. V. Sabadasch, M. Dirksen, P. Fandrich, and T. Hellweg, "Multifunctional Core-Shell Microgels as Pd-Nanoparticle Containing Nanoreactors with Enhanced Catalytic Turnover," *Frontiers in Chemistry* 10 (2022).

24. S. Wu, J. Dzubiella, J. Kaiser, et al., "Thermosensitive Au-PNIPA Yolk–Shell Nanoparticles with Tunable Selectivity for Catalysis," *Angewandte Chemie International Edition* 51, no. 9 (2012): 2229–2233.

25. N. Welsch, M. Ballauff, and Y. Lu, "Microgels as Nanoreactors: Applications in Catalysis," in *Chemical Design Of Responsive Microgels*, ed. A. Pich and W. Richtering (Springer, Berlin, Heidelberg 2010), 129–163.

26. A. Pich, A. Karak, Y. Lu, A. K. Ghosh, and H.-J. P. Adler, "Preparation of Hybrid Microgels Functionalized by Silver Nanoparticles," *Macromolecular Rapid Communications* 27, no. 5 (2006): 344–350.

27. D. Suzuki and H. Kawaguchi, "Modification of Gold Nanoparticle Composite Nanostructures Using Thermosensitive Core−Shell Particles as a Template," *Langmuir* 21 (2005): 8175–8179.

28. M. Das, N. Sanson, D. Fava, and E. Kumacheva, "Microgels Loaded with Gold Nanorods: Photothermally Triggered Volume Transitions under Physiological Conditions," *Langmuir* 23, no. 1 (2007): 196–201.

29. J. Siirilä, M. Karesoja, P. Pulkkinen, J.-M. Malho, and H. Tenhu, "Soft Poly(N-vinylcaprolactam) Nanogels Surface-Decorated with AuNPs. Response to Temperature, Light, and RF-Field," *European Polymer Journal* 115 (2019): 59–69.

30. V. R. R. Kumar, A. K. Samal, T. S. Sreeprasad, and T. Pradeep, "Gold Nanorods Grown on Microgels Leading to Hexagonal Nanostructures," *Langmuir* 23, no. 17 (2007): 8667–8669.

31. M. Karg, I. Pastoriza-Santos, J. Pérez-Juste, T. Hellweg, and L. M. Liz-Marzán *Nanorod-Coated PNIPAM Microgels: Thermoresponsive Optical Properties* 3, no. 7 (2007): 1222–1229.

32. Y. Zhang, K. Liu, Y. Guan, and Y. Zhang, "Assembling of Gold Nanorods on P(NIPAM–AAPBA) Microgels: a Large Shift in the Plasmon Band and Colorimetric Glucose Sensing," *RSC Advances* 2, no. 11 (2012): 4768.

33. Q. M. Zhang, D. Berg, S. M. Mugo, and M. J. Serpe, "Lipase-Modified pH-Responsive Microgel-Based Optical Device for Triglyceride Sensing," *ChemComm* 51, no. 47 (2015): 9726–9728.

34. M. Müller, M. Tebbe, D. V. Andreeva, et al., "Large-Area Organization of pNIPAM-Coated Nanostars as SERS Platforms for Polycyclic Aromatic Hydrocarbons Sensing in Gas Phase," *Langmuir* 28, no. 24 (2012): 9168–9173.

35. C. D. Jones and L. A. Lyon, "Photothermal Patterning of Microgel/Gold Nanoparticle Composite Colloidal Crystals," *Journal of the American Chemical Society* 125, no. 2 (2003): 460–465.

36. M. Dulle, S. Jaber, S. Rosenfeldt, et al., "Plasmonic Gold–poly(N-isopropylacrylamide) Core–shell Colloids with Homogeneous Density Profiles: a Small Angle Scattering Study," *Physical Chemistry Chemical Physics* 17, no. 2 (2015): 1354–1367.

37. B. Sharma and S. Striegler, "Crosslinked Microgels as Platform for Hydrolytic Catalysts," *Biomacromolecules* 19, no. 4 (2018): 1164–1174.

38. Y. Lu, Y. Mei, M. Drechsler, and M. Ballauff, "Thermosensitive Core–Shell Particles as Carriers for Ag Nanoparticles: Modulating the Catalytic Activity by a Phase Transition in Networks," *Angewandte Chemie International Edition* 45, no. 5 (2006): 813–816.

39. M. Karg, "Functional Materials Design through Hydrogel Encapsulation of Inorganic Nanoparticles: Recent Developments and Challenges," *Macromolecular Chemistry and Physics* 217, no. 2 (2016): 242–255.

40. M. Karg, T. Hellweg, and P. Mulvaney, "Self-Assembly of Tunable Nanocrystal Superlattices Using Poly-(NIPAM) Spacers," *Advanced Functional Materials* 21 (2011): 4668–4676.

41. N. Vogel, C. Fernández-López, J. Pérez-Juste, L. M. Liz-Marzán, K. Landfester, and C. K. Weiss, "Ordered Arrays of Gold Nanostructures from Interfacially Assembled Au@PNIPAM Hybrid Nanoparticles," *Langmuir* 28 (2012): 8985–8993.

42. T. Honold, K. Volk, M. Retsch, and M. Karg, "Binary Plasmonic Honeycomb Structures: High-Resolution EDX Mapping and Optical Properties," *Colloids and Surfaces a-Physicochemical and Engineering Aspects* 510 (2016): 198–204.

43. D. Feller, M. Otten, M. S. Dimitriyev, and M. Karg, "Non-Close-Packed Plasmonic Bravais Lattices through a Fluid Interface-Assisted Colloidal Assembly and Transfer Process," *Colloid and Polymer Science* 303 (2025): 1829–1842.

44. D. Feller, J. Wang, J. Kippenberger, et al., "Evolution of Collective, Radiative Plasmon Coupling in Confined, Soft Colloidal Films," *Advanced Optical Materials* (2025): 01657, https://doi.org/10.1002/adom.202501657.

45. E. Ponomareva, K. Volk, P. Mulvaney, and M. Karg, "Surface Lattice Resonances in Self-Assembled Gold Nanoparticle Arrays: Impact of Lattice Period, Structural Disorder, and Refractive Index on Resonance Quality," *Langmuir* 36, no. 45 (2020): 13601–13612.

46. V. G. Kravets, A. V. Kabashin, W. L. Barnes, and A. N. Grigorenko, "Plasmonic Surface Lattice Resonances: a Review of Properties and Applications," *Chemical Reviews* 118, no. 12 (2018): 5912–5951.

47. K. Volk, J. P. S. Fitzgerald, M. Retsch, and M. Karg, "Time-Controlled Colloidal Superstructures: Long-Range Plasmon Resonance Coupling in Particle Monolayers," *Advanced Materials* 27 (2015): 7332–7337.

48. M. Hildebrandt, S. Lazarev, J. Pérez, I. A. Vartanyants, J.-M. Meijer, and M. Karg, "SAXS Investigation of Core–Shell Microgels with High Scattering Contrast Cores: Access to Structure Factor and Volume Fraction," *Macromolecules* 55 (2022): 2959–2969.

49. M. Hildebrandt, D. Pham Thuy, J. Kippenberger, et al., "Fluid–solid Transitions in Photonic Crystals of Soft, Thermoresponsive Microgels," *Soft Matter* 19, no. 37 (2023): 7122–7135.

50. D. Lapkin, N. Mukharamova, D. Assalauova, et al., "In Situ Characterization of Crystallization and Melting of Soft, Thermoresponsive Microgels by Small-Angle X-ray Scattering," *Soft Matter* 18, no. 8 (2022): 1591–1602.

51. A. Rauh, T. Honold, and M. Karg, "Seeded Precipitation Polymerization for the Synthesis of Gold-Hydrogel Core-Shell Particles: the Role of Surface Functionalization and Seed Concentration," *Colloid and Polymer Science* 294 (2016): 37–47.

52. L. S. Zha, Y. Zhang, W. L. Yang, and S. K. Fu, "Monodisperse Temperature-Sensitive Microcontainers," *Advanced Materials* 14, no. 15 (2002): 1090.

53. M. Karg, I. Pastoriza-Santos, L. M. Liz-Marzán, and T. Hellweg, "A Versatile Approach for the Preparation of Thermosensitive PNIPAM Core–Shell Microgels with Nanoparticle Cores," *Chemphyschem* 7, no. 11 (2006): 2298–2301.

54. K. Kuk, L. Gregel, V. Abgarjan, C. Croonenbrock, S. Hänsch, and M. Karg, "Micron-Sized Silica-PNIPAM Core-Shell Microgels with Tunable Shell-To-Core Ratio," *Gels* 8, no. 8 (2022): 516.

55. S. Wu, M. Zhu, Q. Lian, et al., "Plasmonic and Colloidal Stability Behaviours of Au-acrylic Core–shell Nanoparticles with Thin pH-Responsive Shells," *Nanoscale* 10, no. 39 (2018): 18565–18575.

56. M. Karg, S. Jaber, T. Hellweg, and P. Mulvaney, "Surface Plasmon Spectroscopy of Gold−Poly- N -isopropylacrylamide Core−Shell Particles," *Langmuir* 27 (2011): 820–827.

57. S. Thies, P. Simon, I. Zelenina, L. Mertens, and A. Pich, "In Situ Growth and Size Regulation of Single Gold Nanoparticles in Composite Microgels," *Small* 14 (2018): 1803589.

58. P. Mastrorilli, C. F. Nobile, and G. Marchese, "Cobalt(II) and Iron(III) Complexes with 2-(acetoacetoxy)ethylmethacrylate: Potential Precursors of Hybrid Catalysts," *Inorganica Chim Acta* 233, no. 1 (1995): 65–69.

59. M. M. Dell'Anna, P. Mastrorilli, A. Rizzuti, G. P. Suranna, and C. F. Nobile, "Synthesis and Copolymerization of Rhodium(I) and Palladium(II) Complexes with the Deprotonated Form of 2-(acetoacetoxy)ethyl Methacrylate," *Inorganica Chimica Acta* 304, no. 1 (2000): 21–25.

60. T. Honold, K. Volk, A. Rauh, J. P. S. Fitzgerald, and M. Karg, "Tunable Plasmonic Surfaces via Colloid Assembly," *J Mater Chen C* 3, no. 43 (2015): 11449–11457.

61. SasView, https://www.sasview.org/.

62. M. Karg, S. Prévost, A. Brandt, D. Wallacher, R. von Klitzing, and T. Hellweg, "Poly-NIPAM Microgels with Different Cross-Linker Densities," in *Intelligent Hydrogels*, ed. G. Sadowski and W. Richtering (Springer International Publishing, 2013), 63–76.

63. K. Kratz, T. Hellweg, and W. Eimer, "Structural Changes in PNIPAM Microgel Particles as Seen by SANS, DLS, and EM Techniques," *Polymer* 42 (2001): 6631–6639.

64. A. Brézault, V. Schmitt, V. Ravaine, P. Perrin, and N. Sanson, "Limited Aggregation Model″ to Predict the Size of Acrylamide-Based Microgels Synthesized with Ionic Surfactants," *Macromolecular Chemistry and Physics* 225, no. 6 (2024): 2300372.

65. J. D. Debord and L. A. Lyon, "Synthesis and Characterization of pH-Responsive Copolymer Microgels with Tunable Volume Phase Transition Temperatures," *Langmuir* 19, no. 18 (2003): 7662–7664.

66. K. Kratz, T. Hellweg, and W. Eimer, "Influence of Charge Density on the Swelling of Colloidal Poly(-isopropylacrylamide-co-acrylic acid) Microgels," *Colloids and Surfaces a-Physicochemical and Engineering Aspects* 170, no. 2-3 (2000): 137–149.

67. R. Pelton and T. Hoare, "Microgels and Their Synthesis: An Introduction," in *Microgel Suspensions*, eds. A. Fernandez-Nieves, H. M. Wyss, J. Mattsson and D. A. Weitz (Wiley, 2011), 1–32.

68. M. Otten, M. Hildebrandt, B. Pfeffing, et al., "Volume Phase Transition of Thermoresponsive Microgels Scrutinized by Dynamic Light Scattering and Turbidity: Correlations Depend on Microgel Homogeneity," *Langmuir* 40, no. 28 (2024): 14515–14526.

69. E. Ponomareva, B. Tadgell, M. Hildebrandt, et al., "The Fuzzy Sphere Morphology Is Responsible for the Increase in Light Scattering during the Shrinkage of Thermoresponsive Microgels," *Soft Matter* 18, no. 4 (2022): 807–825.

70. D. Gibson, B. F. G. Johnson, and J. Lewis, "Metal β-diketone Complexes. Part VI. Some β-diketone Complexes of Copper(I), Silver(I), and Gold(I)," *Journal of the Chemical Society A: Inorganic, Physical, Theoretical* 000, (1970): 367–369.

71. C. M. Tollan, J. Echeberria, R. Marcilla, J. A. Pomposo, and D. Mecerreyes, "One-Step Growth of Gold Nanorods Using a β-diketone Reducing Agent," *Journal of Nanoparticle Research* 11, no. 5 (2009): 1241–1245.

72. B. Tadgell, E. Ponomareva, M. Karg, and P. Mulvaney, "Scattering of Visible Light by Au–PNIPAM Core–Shell Microgels," *Journal of Physical Chemistry C* 126, no. 36 (2022): 15336–15347.

73. R. Contreras-Cáceres, I. Pastoriza-Santos, R. A. Alvarez-Puebla, J. Pérez-Juste, A. Fernández-Barbero, and L. M. Liz-Marzán, "Growing Au/Ag Nanoparticles within Microgel Colloids for Improved Surface-Enhanced Raman Scattering Detection," *Chemistry - A European Journal* 16 (2010): 9462–9467.

74. N. R. Jana, L. Gearheart, and C. J. Murphy, "Seeding Growth for Size Control of 5–40 Nm Diameter Gold Nanoparticles," *Langmuir* 17, no. 22 (2001): 6782–6786.

75. J. Rodríguez-Fernández, J. Pérez-Juste, F. J. García De Abajo, and L. M. Liz-Marzán, "Seeded Growth of Submicron Au Colloids with Quadrupole Plasmon Resonance Modes," *Langmuir* 22, no. 16 (2006): 7007–7010.

Supporting Information

Additional supporting information can be found online in the Supporting Information section.

Supporting File: macp70125-sup-0001-SuppMat.pdf.